AIAA Aviation Forum and ASCEND co-located Conference Proceedings
29 July - 2 August 2024, Las Vegas, Nevada
AIAA AVIATION FORUM AND ASCEND 2024
10.2514/6.2024-4029

Impact of Coolant Oxidation on the Performance of Evaporative Transpiration Cooling for Sharp Hypersonic Leading Edges

Anthony Mannion*, Danny Ko.†, Y. Sungtaek Ju‡, Xiaolin Zhong§
University of California Los Angeles, Los Angeles, CA, 90095

One of the main limiting design considerations for hypersonic flight vehicles is the severe surface heating experienced during atmospheric hypersonic flights. Surface heat fluxes on the order of 10 MW/m^2 can be expected at hypersonic conditions. State-of-the-art thermal protection systems (TPS), such as ablative heat shields, are limited in that they require blunt geometries and often experience significant surface degradation through material removal. The goal of this study is to examine the use of evaporative transpiration TPS, which do not experience surface degradation as other TPS do. Specifically, this study investigates the effect oxidation of coolant material has on the performance of evaporative transpiration TPS. Three-dimensional direct numerical simulation (DNS) studies are used to simulate the vaporization of coolant material along the leading edge of an evaporative transpiration TPS. The impact of coolant material oxidation under thermochemical nonequilibrium conditions on TPS performance is investigated along the leading edge of a 3.1 mm nose tip radius flying at Mach 15 and an altitude of 30 km. Aluminum is chosen as the coolant material in this study because of its high latent heat of vaporization and low molar mass, as well as aluminum's expected readiness to oxidize at its saturation temperature. The effects of exothermic oxidation reactions on evaporative transpiration TPS are shown to greatly increase the incident heat flux along the leading edge and require over twice the coolant mass flux at the stagnation point to maintain a leading edge temperature near the saturation temperature of the coolant. Additionally, the oxidation reactions consumed all available oxygen in the flow even at artificially lowered reaction rates 10^{-9} times lower than their accepted values. Because oxidation reactions occur so readily and have such a pronounced impact on evaporative transpriation TPS performance, they cannot be neglected. Understanding how coolant oxidation impacts the performance of evaporative transpiration TPS helps design evaporative transpiration TPS capable of providing large cooling fluxes without experiencing surface degradation.

Nomenclature

$C_{f,c}$	=	reaction rate coefficient
c	=	mass fraction
c_p	=	specific heat, J/kg·K
D	=	binary or mixture diffusion coefficient, m^2/s
e	=	specific energy, J/kg
F_j	=	inviscid flux vector
G_j	=	viscous flux vector
h	=	specific enthalpy, J/kg
h_s°	=	species heat of formation, J/kg
K_{eq}	=	equilibrium constant
k	=	thermal conductivity, W/m·K
$k_{f,c}$ and $k_{b,c}$	=	forward and backwards reaction rates
L	=	latent heat of vaporization, J/mol

*PhD Candidate, Mechanincal and Aerospace Engineering Department, ajmannion@g.ucla.edu
†PhD Graduate, Mechanincal and Aerospace Engineering Department
‡Professor, Mechanincal and Aerospace Engineering Department
§Professor, Mechanincal and Aerospace Engineering Department, Associate Fellow AIAA

M	=	molar mass, kg/mol
$\dot{m}$	=	mass flux, kg/m^2·s
P	=	pressure, Pa
Q_{T-v_s}	=	vibrational energy exchange
R	=	universal gas constant, J/mol·K
R_C	=	reaction rate
T	=	temperature, K
U	=	conserved flow variable vector
u_n	=	velocity in n^{th} direction, m/s
W	=	source vector
α	=	accommodation coefficient
$\delta_{i,j}$	=	Kronecker delta
ϵ	=	emissivity
θ	=	non-dimensional temperature
μ	=	viscosity, Pa·s
ν	=	species diffusion velocity, m/s
ρ	=	density, kg/m^3
σ	=	Stefan-Boltzmann constant, 5.670 x 10^{-8} W/(m^{2}K^4)
τ	=	thermochemcial equilibrium time constants
$\tau_{i,j}$	=	viscous stress, Pa
ω	=	rate of species production, kg/(m^{3}s)
Subscripts		
c	=	reaction number
eq	=	equilibrium or saturation
(l)	=	liquid state
n	=	species number
ns	=	total number of species
o	=	stagnation point
T	=	translational-rotational
v	=	vibrational
w	=	wall conditions

I. Introduction

Despite increasing interest in hypersonic flight systems, the practical use of these systems remains limited. One of the main challenges presented by hypersonic flight systems is the severe incident heat loads present during atmospheric hypersonic flight. These extreme heat loads arise during hypersonic flight due to the compressive heating behind the bow shock. Small leading edge radii exacerbate the high incident heat fluxes experienced during hypersonic flight because a linear reduction in leading edge radius leads to a linear increase in the squared incident heat flux [1, 2].

Thermal protection systems (TPS) are used to protect hypersonic vehicles from these high incident heat loads. Current state-of-the-art TPS include ablative heat shields such as those used on the Apollo reentry capsules and passive insulating tiles such as those used on the Space Shuttle. Ablative heat shields are effective at counteracting large incident heat fluxes and can withstand heat fluxes over 30 MW/m^2 [3], though they experience considerable surface degradation as they rely on vaporization of their surface material to absorb the incident heat flux. Blunt shapes must be used with ablative TPS as surface degradation prevents them from maintaining any other geometry. Surface degradation also prevents ablative TPS from being reusable. Passive insulating tiles are not as capable of counteracting incident heat fluxes as ablative heat shields and still require a blunt leading edge to decrease the severity of the incident heat flux.

In addition, post-shock conditions also give rise to such extreme temperatures that there is significant dissociation of air molecules. For example, diatomic oxygen dissociates at 2000 K [4], well below the post-shock temperature for atmospheric hypersonic flight. This creates a highly reactive flow environment as air molecules dissociate, recombine, and react with the leading edge surface. Even passive insulating tiles are not completely reusable, as exposure to these highly reactive conditions degrades the tiles over time.

It is therefore desirable to investigate TPS capable of providing adequate thermal protection without imposing the limitations of current TPS. Evaporative transpiration TPS seek to address these limitations while providing sufficient

thermal protection. Evaporative transpiration TPS continuously supply sacrificial liquid coolant to the leading edge surface where the coolant is vaporized. The vaporization of liquid coolant thereby absorbs the incident heat load during flight in a process similar to ablation. Distinct from an ablative TPS, the expended liquid coolant from an evaporative transpiration TPS can be continually replenished through a porous leading edge. The vapor/liquid coolant layer thereby physically shields the leading edge from high external temperatures and highly chemically reactive flow fields. In this way, evaporative transpiration TPS do not experience vaporization of the leading edge material itself nor surface degradation along the leading edge. As such, evaporative transpiration TPS eliminates both the requirement for blunt shapes and the single-use limitation of current ablative TPS. The prospective use of sharp leading edge geometry owing to evaporative transpiration TPS could greatly increase lift-to-drag ratios and the maneuverability of hypersonic flight systems. Current studies have shown that evaporative transpiration TPS are as effective as ablative TPS at counteracting incident heat fluxes, with Ko et al. [5] showing that, provided a sufficient coolant mass flux, evaporative transpiration TPS can counteract heat fluxes as high as 85 MJ/m^2 along a 3.1 mm nose tip radius leading edge at Mach 20 and 30 km altitude.

Evaporative transpiration TPS function by injecting liquid coolant along a porous leading edge surface, often made from carbon or silica. The coolant is stored in an internal reservoir, and solid coolant particles may need to be melted inside this reservoir before they flow through the porous leading edge material. The coolant is then drawn through the porous material to the surface by external pressure and capillary action. Once the liquid coolant reaches the surface, it absorbs the incident heat flux and vaporizes, discharging into the hypersonic flow as vapor. A diagram showing the operation of an evaporative transpiration TPS is presented in Figure 1.

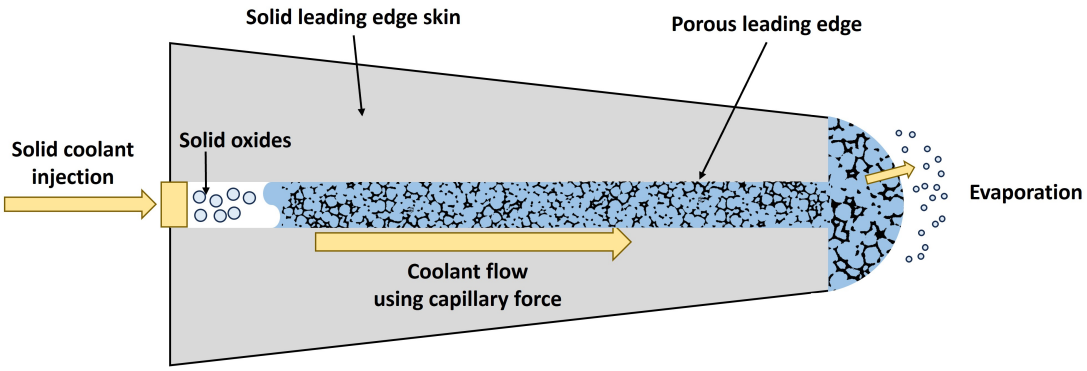

Fig. 1 Example diagram showing how an evaporative transpiration TPS functions. [5]

Previous studies have investigated gases [6–15], water [16], and metals and oxides [5] as prospective coolant materials. Luo et al. [17] showed that liquid coolants are substantially more effective than gaseous coolants as they undergo a phase change along the leading edge surface. Van Foreest et al. [16] conducted experiments using liquid water as the coolant for an evaporative transpiration TPS. This experiment exposed a leading edge to a heat flux of 2.8 MW/m^2, successfully cooling it to less than 300 K using a mass flow rate of only 0.2 g/s of water. While thier work demonstrated the effectiveness of evaporative transpiration TPS at low heat fluxes, much larger heat fluxes must be counteracted during atmospheric hypersonic flight.

Metallic and oxide coolants are capable of counteracting these incident heat fluxes using reasonable coolant mass fluxes due to their high latent heats of vaporization. Metals and oxides also have a wide range of material properties, allowing their use considering a wide range of flight environments and material limits of the leading edge surface. A recent investigation by Ko et al. [5] studied evaporative transpiration TPS through a parametric study on coolant material properties, flight conditions, and nose tip radii. The parametric study was conducted using boundary-layer theory presented by Scala and Vidale [18]. These solutions made use of many simplifying assumptions and were valid only along the stagnation line, so additional DNS solutions were obtained to augment the parametric study. It was found that evaporative transpiration TPS using metallic and oxide coolants ccould withstand heat fluxes up to 85 MW/m^2. It was also determined that oxides are chemically inert when used as the coolant for evaporative transpiration TPS because of their chemically stable nature and the significant presence of oxygen in the flow field, which limits oxide dissociation.

Continuing the work of Ko et al. [5], this study aims to examine the effects of oxidation of metallic coolants on the

performance of evaporative transpiration TPS. Metals oxidize readily at elevated temperatures, and the presence of oxygen in the flow promotes, rather than inhibits, chemical reactions with metallic species. Oxidation reactions are exothermic, and the prevalence of these reactions may increase the temperature of the leading edge past its material limit by raising the surface heat flux. Additionally, coolant oxidation is expected to draw evaporated coolant away from the leading edge surface so that it can react with incoming oxygen. This effect would require larger coolant mass fluxes than cases with no coolant oxidation. Therefore, it is important to understand the physical impact of oxidation reactions on the external flow field and how they affect the performance of evaporative transpiration TPS using metallic coolants. Through DNS studies, the effects of coolant oxidation reactions on the surface heating and the required coolant mass flux of evaporative transpiration TPS are evaluated. The results of this study bring evaporative transpiration TPS a step closer to future implementation.

II. Governing Equations and Models

To accurately detail the effects of metallic coolant oxidation for use in evaporative transpiration TPS, direct numerical simulation (DNS) studies are preferred. DNS solves the complete Naiver-Stokes equations without modeling, making it the most accurate numerical method for studying boundary-layer phenomena. The boundary-layer is of great importance to the study of evaporative transpiration TPS, as the transpiration process occurs almost entirely inside the boundary-layer [18]. Since the performance of transpiration TPS are heavily dependent on boundary-layer phenomena, surface conditions along the leading edge, and diffusive processes, DNS is preferred over simplified models. DNS is used to directly simulate the influence of mass diffusivity, viscosity, and thermal conductivity of the gas phase mixture in the complete Naiver-Stokes equations without any simplifying modeling.

Numerical methods are also a preferred method for studying atmospheric hypersonic flight, as ground test facilities generally rely on expansion waves to accelerate flow to hypersonic conditions. This expansion process creates low enthalpy flows, which impose much lower heat fluxes than those experienced during atmospheric hypersonic flight. Therefore, DNS studies are the preferred method for investigating the performance of evaporative transpiration TPS.

In addition, chemical reactions are extremely important for both atmospheric hypersonic flight, which exhibits substantial dissociation of air species, and evaporative transpiration TPS using metallic coolants, which may involve chemically reactive coolants. As such, a thermochemical nonequilibrium solver is preferred to accurately simulate the time-dependent effects of chemical reactions and vibrational energy exchange, which may occur on a similar timescale as the flow speed.

Aluminum is considered as the metallic coolant for this study. Aluminum has a molar mass of 27 g/mol and a latent heat of vaporization of 319 kJ/mol. The saturation temperature of aluminum at standard temperature and pressure is 2750 K. Due to aluminum's low molar mass and high latent heat of vaporization, it is expected that large incident heat fluxes could be counteracted with minimal coolant mass fluxes of aluminum [5]. In addition, oxidation reactions of aluminum are relatively well-documented, allowing for more accurate solutions of the relevant reactions. This is important because it is currently unknown whether the oxidation reactions will behave as though they are in a frozen state, a non-equilibrium state, or an equilibrium state. At the flow temperatures present in these solutions, aluminum is expected to oxidize readily with the supply of oxygen provided by the free stream.

Therefore, three-dimensional DNS studies are conducted for an evaporative transpiration TPS using aluminum coolant, considering thermochemical nonequilibrium. An altitude of 30 km and a Mach number of 15 are chosen as the flight condition for this study. This flight condition aligns with the center of the flight conditions considered by Ko et al. [5] and corresponds to a point on a curve of typical flight trajectories of hypersonic vehicles from [4]. The nose radius considered in this study is 3.1mm, once again matching the study of Ko et al. [5]. The DNS algorithms consider the Naiver-Stokes equations formulated for 7 species (O_2, N_2, NO, AlO, N, O, Al). Thermochemical nonequilibrium is accounted for using a two temperature model to represent translational-rotational energy and vibrational energy. The conservative three-dimensional Navier-Stokes equations are then formulated for a total of 7 species conservation equations, 3 momentum conservation equations in the x,y, and z directions, the total energy conservation equation, and the vibrational energy conservation equation. The governing equations can be expressed in vector form as:

$$\frac{\partial U}{\partial t} + \frac{\partial F_j}{\partial x_j} + \frac{\partial G_j}{\partial x_j} = W \tag{1}$$

In equation 1, U represents the state vector of conserved quantities, F_j represents the inviscid flux vector, G_j represents the viscous flux vector, and W represents the source terms of each conserved quantity such that:

$$U = \begin{bmatrix} \rho_1 \\ \dots \\ \rho_{ns} \\ \rho u_1 \\ \rho u_2 \\ \rho u_3 \\ \rho e \\ \rho e_v \end{bmatrix} \quad F_j = \begin{bmatrix} \rho_1 u_j \\ \dots \\ \rho_{ns} u_j \\ \rho u_1 u_j + p\delta_{1j} \\ \rho u_2 u_j + p\delta_{2j} \\ \rho u_3 u_j + p\delta_{3j} \\ (p + \rho e)u_j \\ \rho e_v u_j \end{bmatrix}$$

$$G_j = \begin{bmatrix} \rho_1 v_{1j} \\ \dots \\ \rho_{ns} v_{nsj} \\ -\tau_{1j} \\ -\tau_{2j} \\ -\tau_{3j} \\ -u_i \tau ij - k_T \frac{\partial T}{\partial x_j} - k_v \frac{\partial T_v}{\partial x_j} + \sum_{s=1}^{nms} \rho_s h_s v_{sj} \\ -k_v \frac{\partial T_v}{\partial x_j} + \sum_{s=1}^{nms} \rho_s h_s v_{sj} \end{bmatrix} \tag{2}$$

$$W = \begin{bmatrix} \omega_1 \\ \dots \\ \omega_{ns} \\ 0 \\ 0 \\ 0 \\ 0 \\ \sum_{s=1}^{nms} (Q_{T-v_s} + \omega_s e_{v,s}) \end{bmatrix}$$

A. Thermochemcial Nonequilibrium and Material Properties

The reactions contributing to dissociation and recombination of each species are:

$$\mathrm{N_2 + M \longrightarrow 2\,N + M} \tag{R1}$$
$$\mathrm{O_2 + M \longrightarrow 2\,O + M} \tag{R2}$$
$$\mathrm{NO + M \longrightarrow N + O + M} \tag{R3}$$
$$\mathrm{AlO + M \longrightarrow Al + O + M} \tag{R4}$$
$$\mathrm{N_2 + O \longrightarrow NO + N} \tag{R5}$$
$$\mathrm{NO + O \longrightarrow N + O_2} \tag{R6}$$
$$\mathrm{N_2 + O_2 \longrightarrow 2\,NO} \tag{R7}$$

Reactions (*R1*)-(*R4*) are dissociation reactions, and reactions (*R5*)-(*R6*) are exchange reactions. The reaction rates, R_c, for the dissociation reactions are:

$$R_c = \sum_{s=1}^{NS} \left(- k_{f,c,s} \frac{\rho_{r_1}}{M_{r_1}} \frac{\rho_s}{M_s} + k_{b,c,s} \frac{\rho_{p_1}}{M_{p_1}} \frac{\rho_{p_2}}{M_{p_2}} \frac{\rho_s}{M_s} \right) \tag{3}$$

The reaction rates for the exchange reactions are:

$$R_c = -k_{f,c} \frac{\rho_{r_1}}{M_{r_1}} \frac{\rho_{r_2}}{M_{r_2}} + k_{b,c} \frac{\rho_{p_1}}{M_{p_1}} \frac{\rho_{p_2}}{M_{p_2}} \tag{4}$$

The forward and backwards components of each reaction, $k_{f,c}$ and $k_{b,c}$, are:

$$\begin{aligned} k_{f,c} &= C_{f,c} T_a^{\eta_c} \exp(-\theta_d / T_a) \\ k_{b,c} &= k_{f,c} / K_{eq} \end{aligned} \tag{5}$$

The forward reaction rates are computed from [19–22]. The equilibrium constants calculated based on curve fits made from [20], [23], and NIST-JANAF tables [24].

The vibrational energy per unit volume is:

$$\rho e_v = \sum_{s=1}^{NDS} \rho_s e_{v,s} = \sum_{s=1}^{NDS} \rho_s \left(\sum_{m=1}^{NMOD} \frac{g_{s,m} R}{M_s} \frac{\theta_{v,s,m}}{exp(\theta_{v,s,m}/T_v) - 1} \right) \tag{6}$$

$g_{s,m}$ is the degeneracy of each vibrational mode. NDS and $NMOD$ refer to the number of molecular species and the number of vibrational modes of each species, respectively. The characteristic vibrational temperatures and their degeneracies are taken from [20]. The vibrational characteristics of aluminum oxide is set equal to that of silicon oxide from [22] due to lack of better available characteristics. To determine the source term in the vibrational energy the Landau-Teller expression is used:

$$Q_{T-v,s} = \rho_s \frac{e_{v,s}(T) - e_{v,s}(T_v)}{< \tau_s > + \tau_{cs}} \tag{7}$$

Blottner's relationship [25] is used to determine the viscosity and thermal conductivity of air and aluminum. The coefficients from Blottner et al. [25] and Gupta et al. [26] are used for air species. The evaporating species transport properties are estimated using kinetic theory from Hirschfelder et al. [27]. The kinetic diameter of aluminum vapor is estimated based on data presented by Breck [28]. Wilke's semi-empirical relationships [29] is then used to calculate the viscosity and thermal conductivity of the mixture. Finally, to determine the mixture diffusivity, a constant Schmidt number of 0.5 is assumed, as in [30].

B. Numerical Model

A high-order accuracy shock-fitting algorithm developed by [30, 31] is used for spatial-discretization. The coordinate system undergoes a transformation from the Cartesian coordinate system, (x, y, z, t) to the shock fitted coordinate system (ξ, η, ζ, τ) parallel, normal, and tangential to the leading edge surface.

$$\begin{bmatrix} \frac{\partial}{\partial x} \\ \frac{\partial}{\partial y} \\ \frac{\partial}{\partial z} \\ \frac{\partial}{\partial t} \end{bmatrix} = \begin{bmatrix} \xi_x & \eta_x & \zeta_x & 0 \\ \xi_y & \eta_y & \zeta_y & 0 \\ \xi_z & \eta_z & \zeta_z & 0 \\ 0 & \eta_t & 0 & 1 \end{bmatrix} \begin{bmatrix} \frac{\partial}{\partial \xi} \\ \frac{\partial}{\partial \eta} \\ \frac{\partial}{\partial \zeta} \\ \frac{\partial}{\partial \tau} \end{bmatrix} \text{ and } \begin{bmatrix} \frac{\partial}{\partial \xi} \\ \frac{\partial}{\partial \eta} \\ \frac{\partial}{\partial \zeta} \\ \frac{\partial}{\partial \tau} \end{bmatrix} = \begin{bmatrix} x_\xi & y_\xi & z_\xi & 0 \\ x_\eta & y_\eta & z_\eta & 0 \\ x_\zeta & y_\zeta & z_\zeta & 0 \\ x_\tau & y_\tau & z_\tau & 1 \end{bmatrix} \begin{bmatrix} \frac{\partial}{\partial x} \\ \frac{\partial}{\partial y} \\ \frac{\partial}{\partial z} \\ \frac{\partial}{\partial t} \end{bmatrix} \tag{8}$$

The Naiver-Stokes equations in the transformed coordinates are rewritten as:

$$\frac{1}{J} \frac{\partial U}{\partial \tau} + \frac{\partial E'}{\partial \xi} + \frac{\partial F'}{\partial \eta} + \frac{\partial G'}{\partial \zeta} + \frac{\partial E'_v}{\partial \xi} + \frac{\partial F'_v}{\partial \eta} + \frac{\partial G'_v}{\partial \zeta} + U \frac{\partial (1/J)}{\partial \tau} = \frac{W}{J} \tag{9}$$

with:

$$
\begin{aligned}
E' &= \frac{F_1\xi_x + F_2\xi_y + F_3\xi_z}{J} \\
F' &= \frac{F_1\eta_x + F_2\eta_y + F_3\eta_z}{J} \\
G' &= \frac{F_1\zeta_x + F_2\zeta_y + F_3\zeta_z}{J} \\
E'_v &= \frac{G_1\xi_x + G_2\xi_y + G_3\xi_z}{J} \\
F'_v &= \frac{G_1\eta_x + G_2\eta_y + G_3\eta_z}{J} \\
G'_v &= \frac{G_1\zeta_x + G_2\zeta_y + G_3\zeta_z}{J}
\end{aligned}
\tag{10}
$$

A seven point stencil is then used to discretize the spatial derivatives as:

$$
\frac{\partial f_i}{\partial x} = \frac{1}{hb_i}\sum_{k=-3}^{3} a_{i+k} f_{i+k} - \frac{\alpha}{6!b_i} h^5 \left(\frac{\partial f^6}{\partial^6 x}\right) \tag{11}
$$

with:

$$
\begin{aligned}
a_{i\pm3} &= \pm 1 + \frac{1}{12}\alpha \\
a_{i\pm2} &= \pm 9 + \frac{1}{2}\alpha \\
a_{i\pm1} &= \pm 45 + \frac{5}{4}\alpha \\
a_i &= -\frac{5}{3}\alpha \\
b_i &= 60
\end{aligned}
\tag{12}
$$

where α is a term representing the artificial dissipation.

For simulations without reacting coolant, a 3rd-order Runge-Kutta timestepping algorithm developed by [32] is used to advance the solution in time. Oxidation reactions occur extremely fast however, so to resolve those reactions a 2nd-order trapezoidal scheme by [30] is used.

C. Surface Chemistry and Boundary Conditions

The wall boundary conditions are obtained by taking the surface mass balance for each chemical species:

$$
\dot{m}_s = \rho_s u_n - \rho D_s \frac{\partial c_s}{\partial \eta} \tag{13}
$$

and the energy balance at the surface:

$$
k_T \frac{\partial T}{\partial \eta} + k_v \frac{\partial T_v}{\partial \eta} + \sum_{s=1}^{Ns} \rho h_s D_s \frac{\partial c_s}{\partial \eta} = \sigma \epsilon T^4 + \dot{m} \sum_{s=1}^{Ns} c_s h_{s,0} \tag{14}
$$

where:

$$
h_{s,0} = (c_{v_s} + \frac{R}{M_s})T + e_{v_s} + h_s^\circ + \frac{1}{2}(u_1^2 + u_2^2 + u_3^2) \tag{15}
$$

The energy balance considers the conductive heat flux, the mass diffusion heat flux, and the radiation heat flux. The conductive heat flux into the leading edge surface is considered equal to the energy needed to raise the aluminum to its saturation temperature. k is the thermal conductivity of the mixture, D_s is the diffusivity of each species, c_s is the species mass fraction, h_s is the species enthalpy, $h_{s,0}$ is the stagnation enthalpy of each species, and η is the wall normal direction.

One of the species mass flux equations is substituted for the equation of state of the gas mixture and the resulting system of equations is solved using Newton's iteration method. The pressure gradient at the surface is nonzero owing to the mass flux of vaporizing coolant, and so Lagrange polynomials are used to extrapolate pressure towards the surface as in [30]. For further details about the solution procedure to these boundary conditions, see [30].

The wall mass flux, $\dot{m}_s$, of vaporizing coolant can be obtained using the Hertz-Knudsen equation:

$$\dot{m}_s = \alpha_s \sqrt{\frac{M}{2\pi R T_w}} \left(P_{eq} - P_s \right) \tag{16}$$

P_s is the partial pressure of the vapor and P_{eq} is the saturation pressure of the vapor. α_s is the accommodation coefficient and represents the probability that a molecular collision will lead to a reaction. For vaporization reactions, the accommodation coefficient for liquids has been show to be typically equal to one [18]. The saturation pressure at surface conditions are calculated for using the Clausius-Clapeyron equation:

$$P_{eq} = P^* \exp\left[\frac{L}{R} \left(\frac{1}{T^*} - \frac{1}{T_w} \right) \right] \tag{17}$$

P^* and T^* are the saturation pressure and temperature of aluminum under standard conditions. Additional surface mass fluxes can be determined for reactions between liquid coolant material and gases present at the liquid surface. This study considers only the reactions between atomic oxygen and liquid aluminum. The possible surface reactions considered are:

$$\mathrm{O} + \mathrm{Al}_{(l)} \longrightarrow \mathrm{AlO} \tag{\textit{SR1}}$$

$$\mathrm{O} + \mathrm{O} + \mathrm{Al}_{(l)} \longrightarrow \mathrm{O}_2 + \mathrm{Al}_{(l)} \tag{\textit{SR2}}$$

Reaction *SR2* considers atomic recombination of atomic oxygen at the wall. The heat of reaction is accounted for in equation 14. Reactions with nitrogen are neglected due to the chemically stable nature of diatomic nitrogen and the low presence of atomic nitrogen expected under surface conditions. These surface reactions induce the following surface mass fluxes:

$$\dot{m}_{O_2} = \alpha_s \rho_O \sqrt{\frac{R T_w}{2\pi M_O}} \tag{18}$$

$$\dot{m}_{AlO} = \alpha_s \rho_O \sqrt{\frac{R T_w}{2\pi M_O}} \frac{M_{AlO}}{M_O} \tag{19}$$

$$\dot{m}_O = -2\alpha_s \rho_O \sqrt{\frac{R T_w}{2\pi M_O}} \tag{20}$$

An accommodation coefficient, α_s of one is assumed once again for these reactions.

III. Validation of the Models

The DNS algorithms, chemical reactions, boundary conditions, and vaporization process were previously validated for a 5-species air code, a 6-species code with a non-reacting coolant, and an 11-species code with carbon ablation. The validation of DNS algorithms and the 5-species nonequilibrium code is detailed in [33]. The validation of the 6-sepcies code is detailed in [5]. The validation of the 11-species code is detailed in [30]. The previous validation studies [5], [30], and [33] serve to validate the unchanged portion of the DNS code used in this study.

Changes made to the 6-species code of [5] resulted in a new 7-species code allowing for an additional chemical reaction between the coolant species and atomic oxygen, as well as additional surface mass fluxes as described in [30]. There are currently no experimental solutions available to validate the new 7-species code. Instead, a comparison case is conducted for the new 7-species code with a reaction rate of the new oxidation reaction set to 0. These results are

Table 1 Comparison of stagnation point properties for non-reacting flow solutions.

Property	6-Species	7-Species Non-reacting
Pressure (kpa)	328.6	328.6
Temperature (K)	2646	2647
Density (kg/m^3)	0.375	0.375
Mass Fraction of Al	0.186	0.186
Coolant Mass Flux (kg/m^2-s)	0.986	0.987
Incident Heat Flux (MW/m^2)	15.05	15.06
Evaporative Heat Flux (MW/m^2)	13.66	13.67
Radiation Heat Flux (MW/m^2)	1.389	1.391

compared to the previously validated 6-species code considering the same coolant material. The comparison shows proper implementation of all new algorithms in the new code. The comparison is shown in table 1.

The difference between the 6-species and 7-species solutions for non-reacting coolants is small, less than 0.1% for flow variables and surface heat and mass fluxes. The differences are small enough that they are suspected to be due to the extra species conservation equation, the different time-stepping algorithms used in each code, the iterative procedure inside the boundary conditions, and the different time convergence history. These small and explainable differences serve to validate the changes made to create the 7-species code. Contour plots of the mass fraction of aluminum for the non-reacting 6 and 7-species solutions are presented in figure 2.

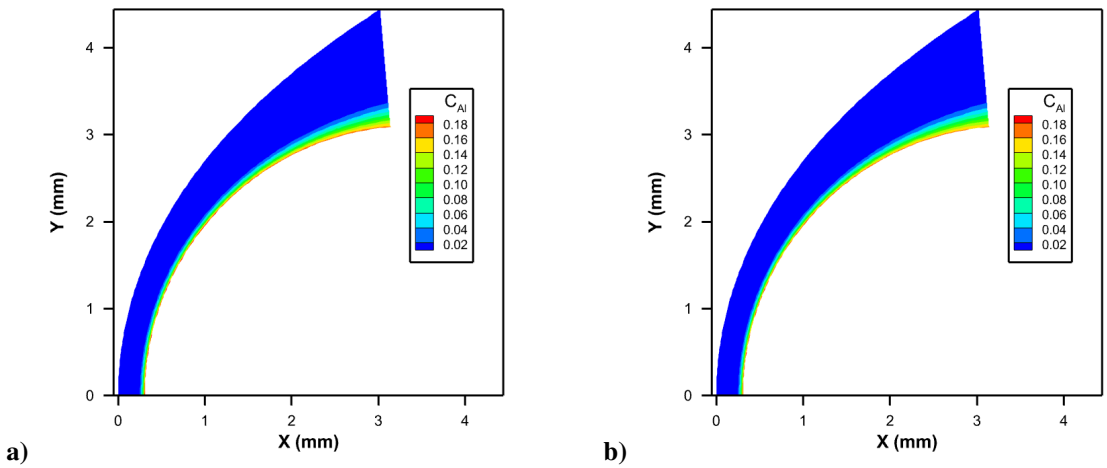

Fig. 2 Contour plots of non-reacting *Al* coolant using 6-species (left) and 7-species (right) solutions.

The reaction rate is then slowly increased in the 7-species code and the surface reactions are enabled to verify the new reactions are implemented correctly. The solutions show proper conservation of mass and energy principles. Additionally, the reaction rates are confirmed to vary with temperature as described in established literature [19–24] showing proper implementation of the reaction curve fits. These checks provide confidence in the accuracy of the code and serve as validation for the changes made to the DNS code in the absence of experimental results to compare with.

Additionally, a grid refinement study is performed considering grid sizes of 30x80, 60x160, 120x320, and 240x640 grid points. The results showed that there is at most a 0.33% difference in the stagnation point pressure among the different grid sizes studied. The 120x320 grid size is used in this study for high-resolution solutions inside the boundary-layer. Solutions are obtained using Purdue's ANVIL high-performance computing clusters, which consist of compute nodes with 128 cores per socket. The solutions are run from previously converged solutions published in [5], which considered similar coolant materials. This provided an initial guess close to converged results and reduced the

computational time needed to reach converged solutions.

IV. Impact of Coolant Vapor Oxidation

In order to determine the effect of coolant oxidation on the performance of evaporative transpiration TPS, a 7-species study is conducted considering oxidation of aluminum coolant vapor. Figure 3 shows contour plots of temperature for the 6 and 7-species solutions. Figure 4 shows a comparison of the mass fractions of reacting species along the stagnation line between the 6 and 7-species solutions, while Figure 5 shows a comparison of the temperature and vibrational temperature along the stagnation line between the 6 and 7-species solutions. The distance along the stagnation line has been normalised by the standoff distance of the shock in Figures 4 and 5. In these figures, the left and right bounds of the plotting regions are the post-shock and surface locations respectively.

A region of elevated temperature can be observed in the 7-species solution in Figures 3 and 5 that is not present in the 6-species solution. The flow temperature is about 2500 K hotter at this location in the 7-species solution. The peak temperature of this region of elevated temperature occurs at a normalised distance of 0.94 along the stagnation line, or approximately 20 micrometers from the surface in physical length. The location of the region of elevated temperature observed in Figure 5 occurs at the same location as peak aluminum oxide concentration in Figure 4. This indicates that the region of elevated temperature is caused by the energy released through the exothermic oxidation reaction of aluminum and the resulting formation of aluminum oxide.

Figure 6 presents contour plots of the mass fractions of aluminum species in the 7-species solutions. This figure also shows streamlines as white lines. This plot is zoomed in near the stagnation point to better illustrate the species concentration profiles. The left and right bounds of the contour regions are the post-shock and surface locations respectively.

Figures 4 and 6 show the stagnation point mass fraction of aluminum to be equal to 0.173 for the 7-species solutions, which is 7% lower than the 6-species solution. This result is counterintuitive as the exothermic oxidation reaction should increase the incident heat flux and require more coolant mass flux as a result. A larger coolant mass flux should raise the surface concentration of coolant. While the oxidation reaction does consume aluminum in the 7-species solutions, there is also a large presence of aluminum oxide at the stagnation point in these solutions. Figures 4 and 6 show a stagnation point mass fraction of 0.34 aluminum oxide. The high mass fraction of the relatively heavy aluminum oxide and the consumption of the additional supply of aluminum to produce this oxide decreases the surface concentration of aluminum vapor.

Table 2 presents important flow variables and the surface mass and heat fluxes for the 6 and 7-species solutions at the stagnation point. Additionally, a 6-species solution is shown considering a coolant identical to non-reacting aluminum but with only one-third of the latent heat of vaporization of aluminum. This additional solution is obtained to better characterize the effect of coolant oxidation on the performance of an evaporative transpiration TPS. A previous study, [5], shows predictions for how coolant properties alter evaporative transpiration TPS performance. Using the results from [5], it is determined that the required coolant mass flux of aluminum is approximately equal to that of a chemically inert species with one-third of the latent heat of vaporization of aluminum.

Table 2 Comparison of stagnation point flow properties

Property	6-species	7-Species Reacting	6-species 1/3rd h_s°
Pressure (kpa)	328.6	328.6	328.6
Temperature (K)	2646	2681	2656
Density (kg/m^3)	0.375	0.465	0.468
Mass Fraction of Al	0.186	0.173	0.364
Coolant Mass Flux (kg/m^2-s)	0.986	2.23	2.20
Incident Heat Flux (MW/m^2)	15.05	32.38	13.81
Evaporative Heat Flux (MW/m^2)	13.66	30.91	12.40
Radiation Heat Flux (MW/m^2)	1.389	1.464	1.410

Table 2 demonstrates that the coolant oxidation reaction raises the stagnation temperature to 2681 K, a 1.3% increase

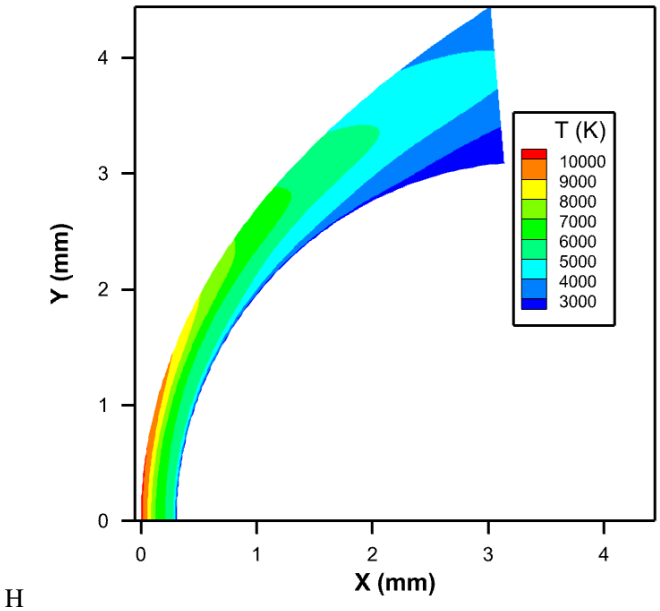

H

a)

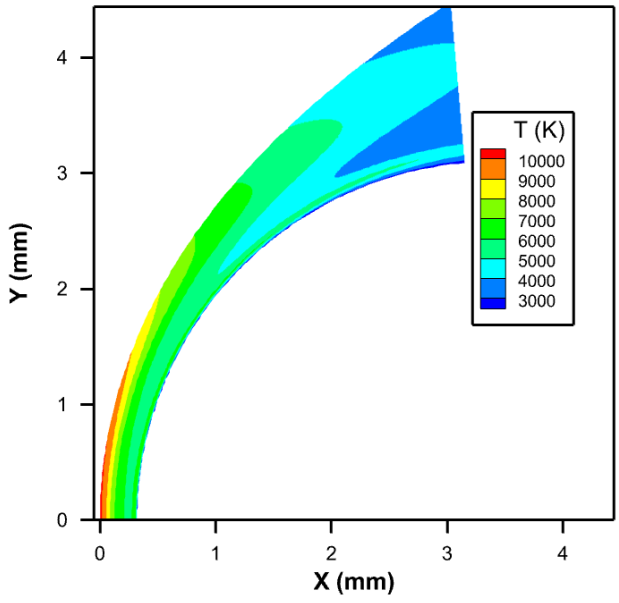

b)

Fig. 3 Contour plots of temperature for 6-species (top) and 7-species (bottom) solutions.

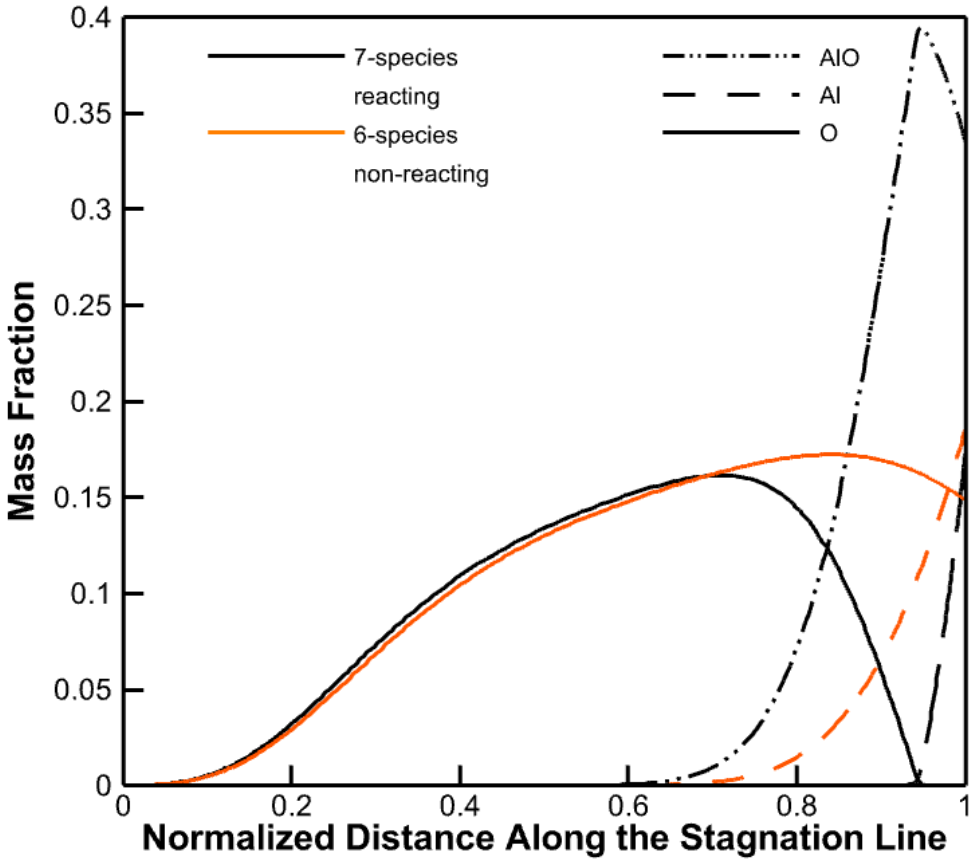

Fig. 4 Normalized stagnation line profile of species mass fractions for 6 and 7-species solutions.

from the non-reacting 6-species solution. An increase in surface temperature is expected due to the increased heating from the exothermic oxidation reaction. However, there is an exponential relationship between the surface temperature and the mass flux as shown by equations 16 and 17. As such, the surface temperature will remains near the saturation temperature of aluminum, as even a small increase in the surface temperature in equation 17 greatly raises the evaporate mass flux in equation 16. A small mass flux of vaporizing coolant can provide a large evaporative heat flux, and so for a small increase in surface temperature, a large evaporative heat flux cools the surface. This phenomenon keeps the surface temperature of an evaporative transpiration TPS near the saturation temperature of its coolant. This result has been observed in previous studies such as [5, 16].

The coolant oxidation reaction increases the coolant mass flux to 2.23 kg/m^2-s, a 126% increase over the non-reacting 6-species solution. This is because the exothermic oxidation reaction creates the region of elevated temperature as observed in Figure 5. The region of elevated temperature increases the temperature gradient inside the boundary-layer significantly, thereby increasing the incident heat flux and required evaporative heat flux. A larger evaporative heat flux can only be supplied by increasing the coolant mass flux. As a result, the 7-species solutions show a roughly twofold increase in the coolant mass flux and the evaporative heat flux at the stagnation point. Because the surface temperature between the 6 and 7-species solutions are similar, the radiation heat fluxes also remain similar.

The solution for a coolant with one-third of the latent heat of vaporization of aluminum shows the expected twofold increase in the stagnation point mass flux as shown in Table 2. Worth noting is the decrease in both the incident heat flux and evaporative heat flux for this solution when compared to the original 6-species solution. [5] has shown that coolants with smaller latent heats of vaporization create smaller thermal gradients inside the boundary-layer. As such,

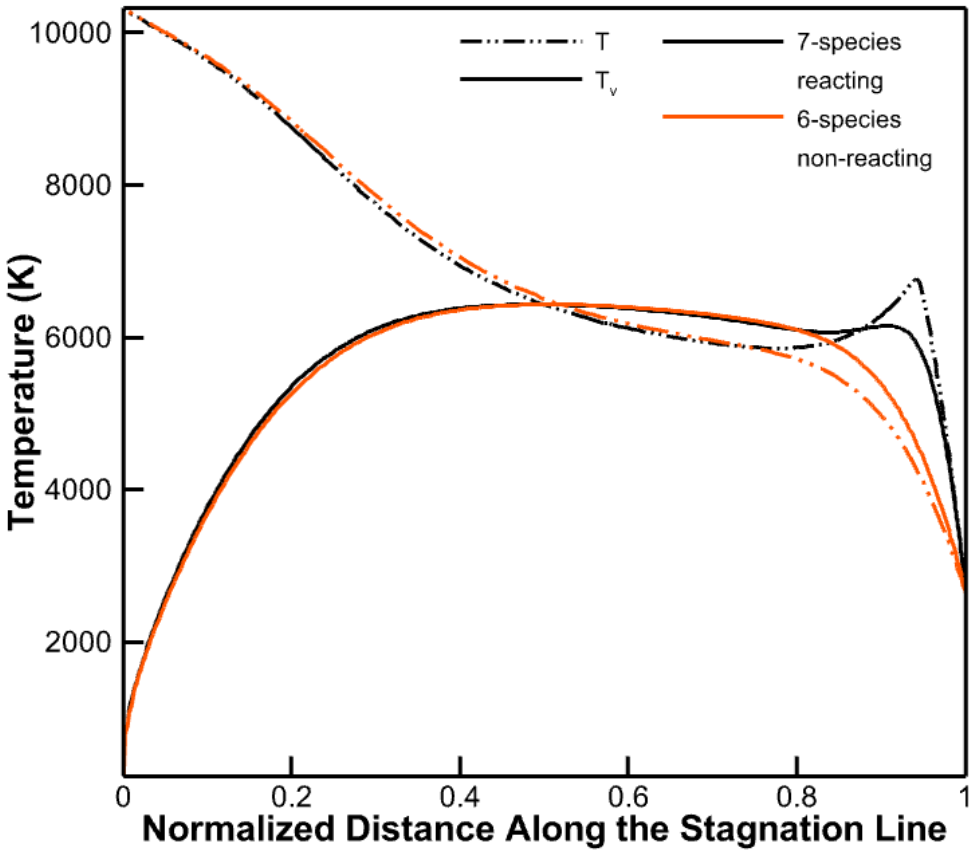

Fig. 5 Normalized stagnation line profile of temperature and vibrational temperature for 6 and 7-species solutions.

both the incident and evaporate heat flux decrease with decreasing latent heat of vaporization. Table 2 also shows that the mass fraction of aluminum for the one-third latent heat of vaporization solution is larger than those for all other solutions. This is due to the larger coolant mass flux required of the less potent coolant material used in the one-third latent heat of vaporization solution.

As for the performance changes caused by coolant oxidation, Table 2 shows a roughly twofold increase in required coolant mass flux at the stagnation point between the 6 and 7-species solutions. As discussed, this is equivalent to a roughly one-third reduction in coolant latent heat of vaporization. The performance drawbacks of using a coolant susceptible to oxidation are significant, and the effects of oxidation must be accounted for during design. Due to its low molar mass and high latent heat of vaporization, aluminum as a coolant material remains competitive when compared to other similar coolants studied in [5]. Other coolants that undergo oxidation may still prove useful should they have low enough molar masses or high enough latent heats of vaporization to compensate for their decreased cooling efficiency.

V. Impact of Surface Chemistry

Atomic oxygen is highly reactive, and it is expected that the liquid coolant layer will react readily with atomic oxygen in the flow. Additionally, atomic oxygen can recombine along the relatively cool leading edge surface to form diatomic oxygen. Both of these processes have been shown to be significant in the context of carbon ablation [30], and can affect the incoming surface heating. Therefore, a study considering the oxidation of liquid aluminum coolant and

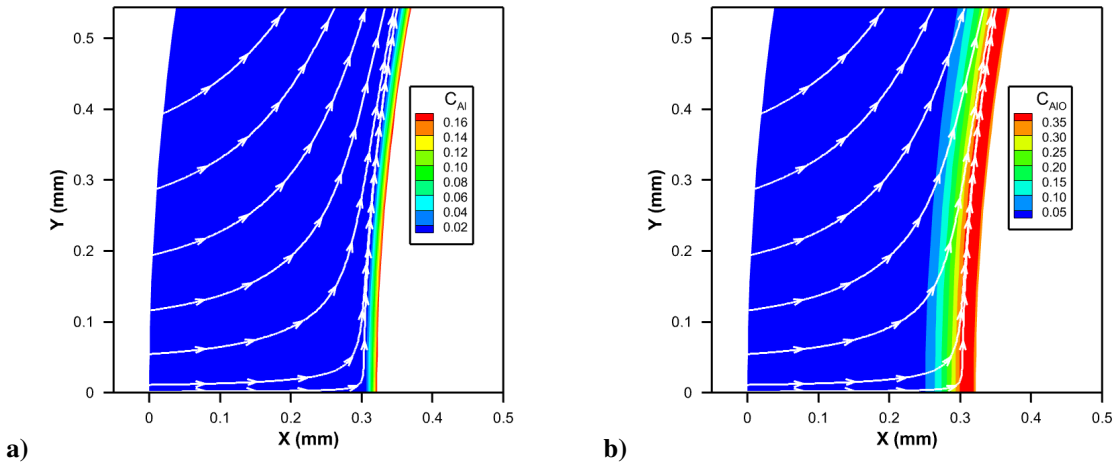

Fig. 6 Contour plots for 7-species mass fractions of *Al* (left) and *AlO* (right).

the recombination of atomic oxygen along the leading edge surface is warranted. The effects of these surface reactions on the performance of an aluminum transpiration TPS are explored in this section.

Figure 7 presents contour plots of the mass fractions of atomic oxygen from the 7-species solutions for both non-reacting and reacting surface chemistry as governed by equations 18, 19, and 20. This plot is zoomed in close to the stagnation point to better illustrate the species concentration profiles. Streamlines are once again shown as white lines. The left and right bounds of the contour regions are the post-shock and surface locations respectively.

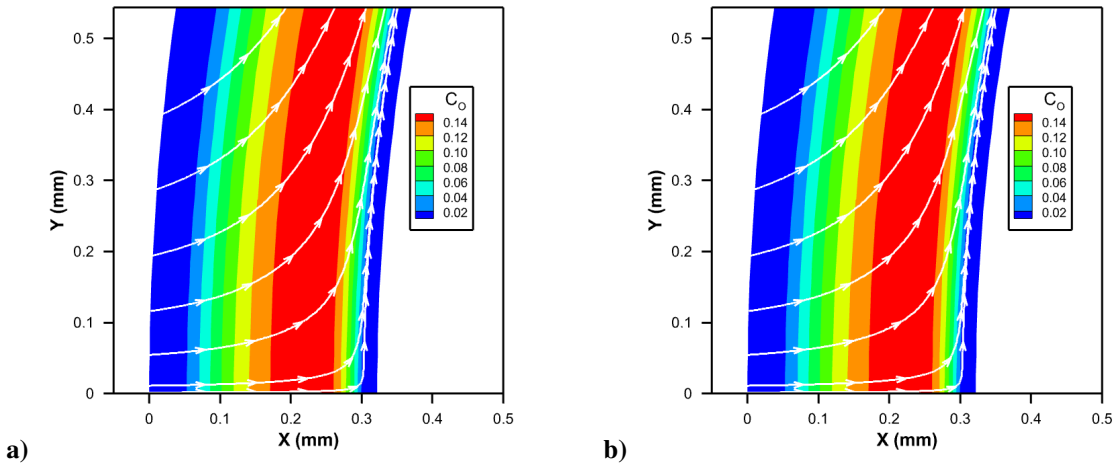

Fig. 7 Contour plots for mass fractions of *O* considering 7-species with non-reacting surface chemistry (left) and reacting surface chemistry (right).

Figure 8 shows a comparison of the mass fractions of reacting species along the stagnation line between the solutions with non-reacting and reacting surface chemistry. The distance along the stagnation line has been normalised by the standoff distance of the shock. The left and right bounds of the plotting regions are the post-shock and surface locations respectively.

Figures 7 and 8 both show a stagnation point mass fraction of atomic oxygen equal to 0. This is because all oxygen reacts to form aluminum oxide around the region of elevated temperature, at a normalized distance of about 0.94, or 20 micrometers, from the leading edge surface, as discussed with Figures 4 and 5. Because the diffusion rate of oxygen toward the leading edge surface is negligible compared to the rate of oxygen consumption by the oxidation reaction,

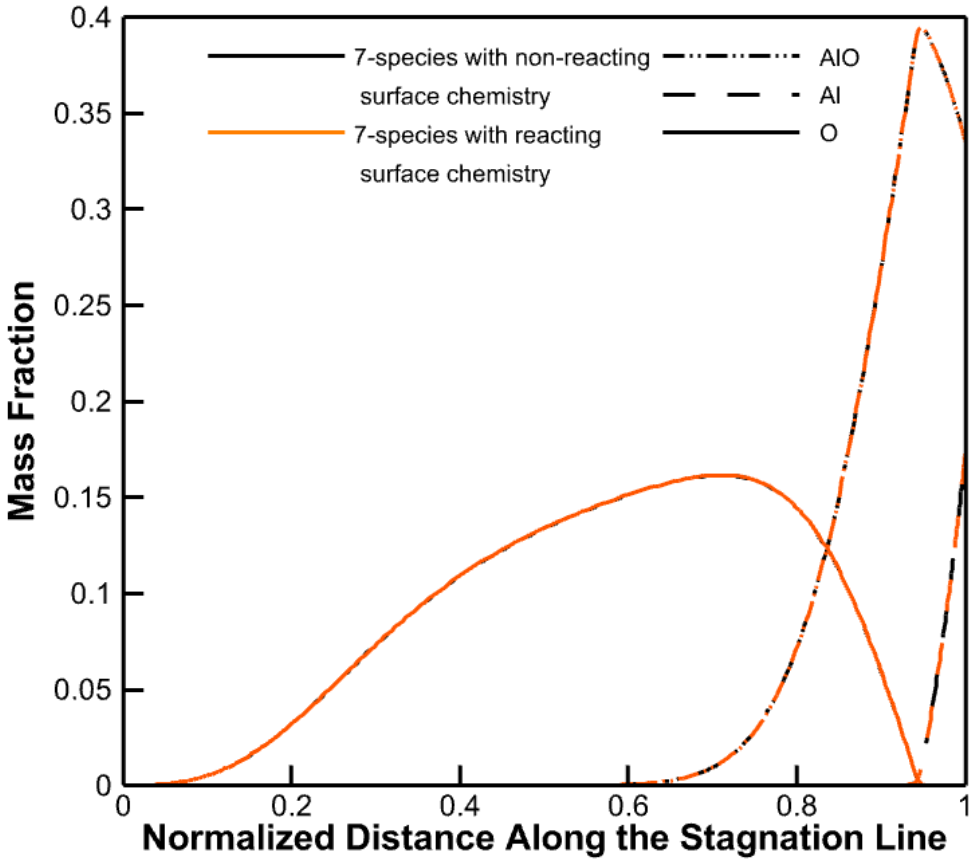

Fig. 8 Normalized stagnation line profile of species mass fractions for 7-species solutions with non-reacting and reacting surface chemistry.

the surface observes no significant oxidation. As a result, the flow variables and the evaporative transpiration TPS performance do not change when considering the oxidation of liquid aluminum coolant and the recombination of atomic oxygen along the leading edge surface. Therefore, it is reasonable to neglect these considerations.

VI. Impact of Reaction Speed

In order to further explore how oxidation reactions behave, a study is conducted varying the reaction rate coefficient, $C_{f,c}$ as found in equation 5, of the aluminum oxidation reaction. The values of the coefficient are varied from their full value of $C_{f,c}$ = 2x10^{10} to a value of 2x10^{-3}. The zero reaction rate of the non-reacting 7-species study from the validation section is included as well.

Figure 9 presents the species mass fraction of reacting species along the stagnation line for the different reaction rates considered. Not all solutions end at the same location, however. This is because the standoff distance of the shock varies as a result of differences in the flow properties caused by the exothermic oxidation reaction. Therefore, the results in Figure 10 are rescaled to be normalized as a percentage of the standoff distance of the shock, allowing for direct comparison between different values of the reaction rate coefficient. Figure 10 presents separate subplots of the species mass fraction of different reacting species. In these figures, the left and right bounds are the post-shock and surface locations respectively.

Figure 10 illustrates that for reaction rate coefficients of 2x10^{4} and greater, there is no substantial change in the

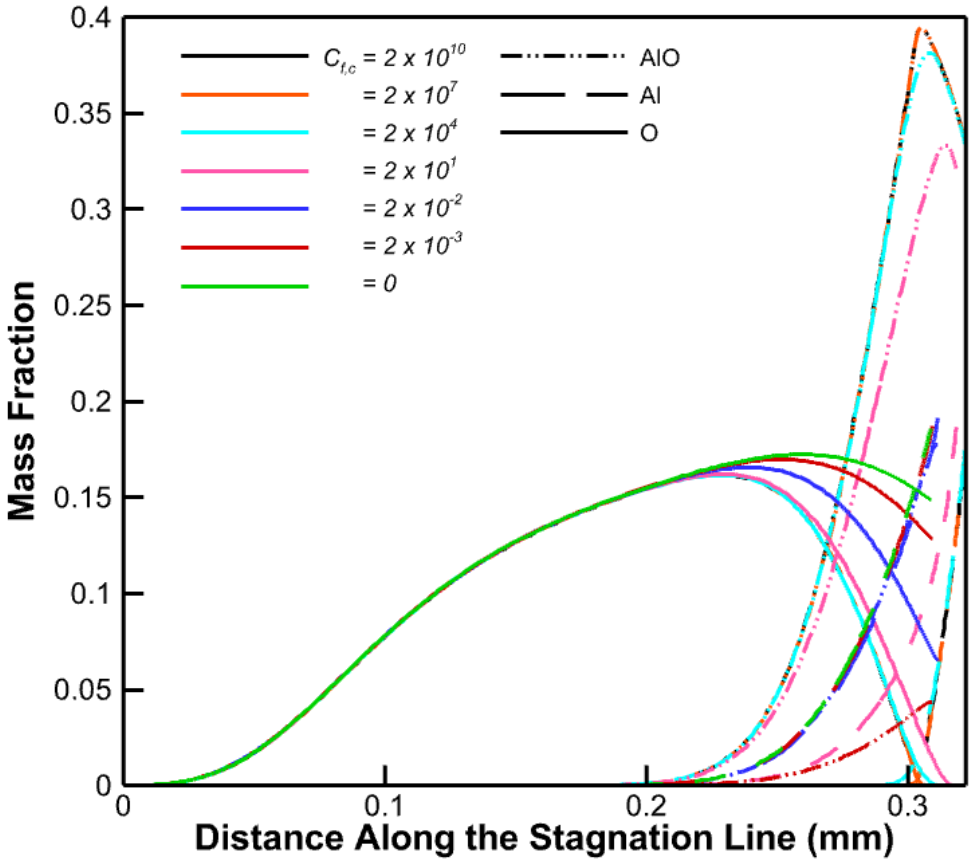

Fig. 9 Stagnation line profile of species mass fractions for different reaction rates.

production of aluminum oxide. For a reaction rate coefficient of $2\text{x}10^1$, a slight decrease in the maximum value of aluminum oxide's mass fraction is observed, and the production center moves closer towards the surface. Additionally, for all solutions with $C_{f,c} > 2\text{x}10^1$, all oxygen in the flow reacts to form aluminum oxide at a normalized distance of about 0.94, or 20 micrometers away from the surface. This observation suggests that the flow variables are not sensitive to increasing the reaction rate coefficient above $C_{f,c} = 2\text{x}10^1$. When considering oxidation of aluminum with values of $C_{f,c} > 2\text{x}10^1$, the flow remains in a state of chemical equilibrium where the reaction kinetics are substantially faster than the flow speeds. This also explains the stiffness of the reactions in the flow solver for $C_{f,c} > 2\text{x}10^4$.

At a value of $C_{f,c} = 2\text{x}10^{-2}$, the reaction kinetics appear to have changed slightly. Oxygen and aluminum coexist with aluminum oxide in a nonequilibrium state at the stagnation point. The stagnation point mass fraction of oxygen is 0.067 as seen in Figure 10. While the presence of oxygen shows that the reaction is progressing slowly in a state of nonequilibrium, the low mass fraction of oxygen suggests that the reaction rate is nearing a state of equilibrium. If the mass fraction of oxygen were zero at the stagnation point, oxygen would have reacted completely, with the reaction reaching equilibrium rather than remaining in a nonequilibrium state.

Moving to a value of $C_{f,c} = 2\text{x}10^{-3}$, the oxidation reaction nearly halts. Only a small amount of aluminum oxide is formed at this reaction rate, with a mass fraction of 0.044 at the stagnation point. Nearly all of the atomic oxygen reaches the surface at this reaction rate. Therefore, $C_{f,c} = 2\text{x}10^{-3}$ can be considered the highest reaction rate value for the oxidation reaction to remain chemically frozen, with results nearly identical to the non-reacting solutions.

The reactions exhibit a dramatic change over a small range of reaction rate coefficient, consuming all oxygen in a chemical equilibrium state for $C_{f,c} \geq 2\text{x}10^1$, but acting chemically inert in a frozen state for $C_{f,c} \leq 2\text{x}10^{-3}$. With a

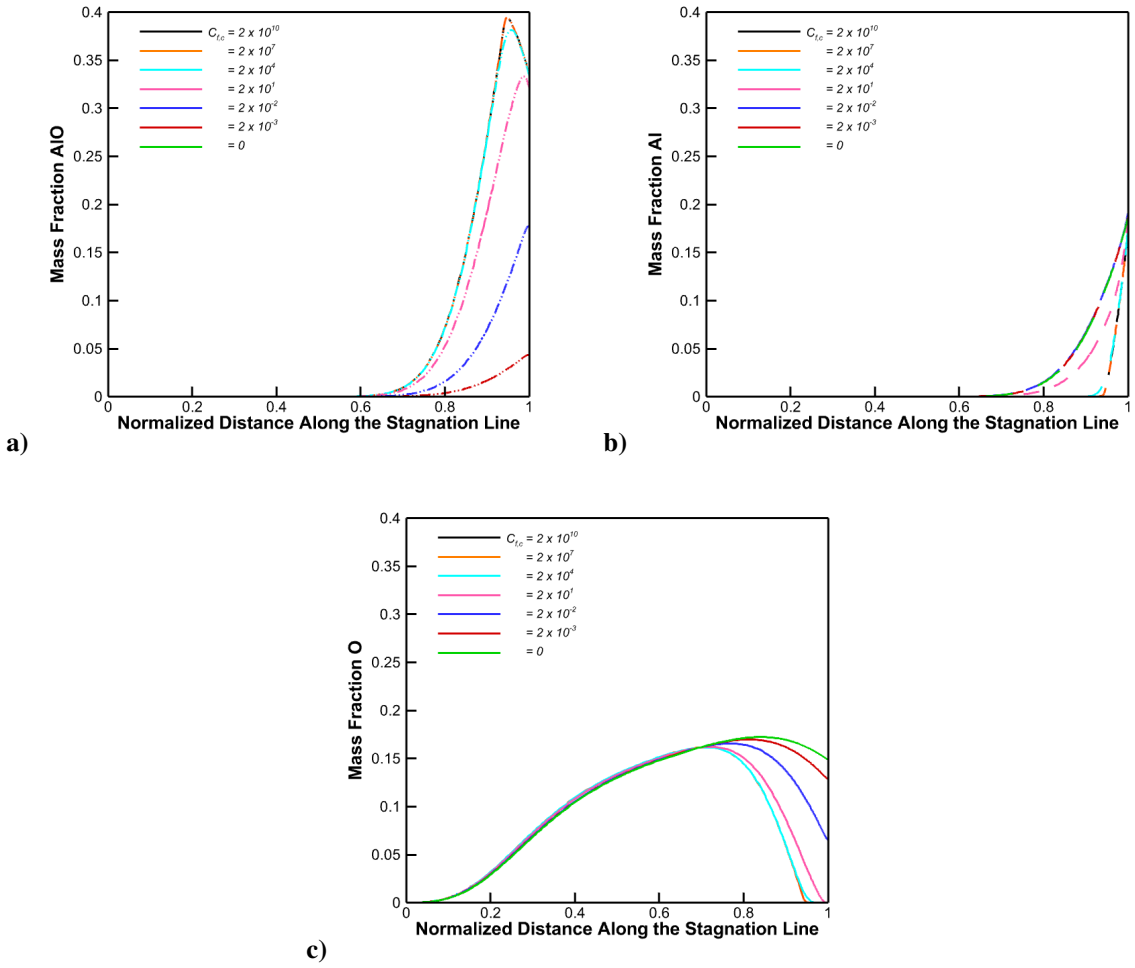

Fig. 10 Normalized stagnation line profile of species mass fractions for varying reaction rates.

slight increase of $C_{f,c}$ = 2x10^{-3} to 2x10^{-2}, the reaction transitions from a frozen state to a nonequilibrium state, closely approaching an equilibrium state. The range of reaction rates where the reaction is in nonequilibrium is so small that it is reasonable to assume that oxidation reactions occur in either equilibrium or frozen conditions.

Then, for a favorable equilibrium constant with reactant species present [5], oxidation reactions act in an equilibrium state for suitably large reaction rates. If these conditions are not met, then the reaction does not occur and can be neglected entirely. For a reaction rate as small as 10^{-9} times lower than its accepted values, oxidation of aluminum coolant occurs in a near-equilibrium state with complete consumption of oxygen species. Even extremely slow oxidation reactions cannot be neglected if their equilibrium constant is large.

Figure 11 presents the temperature and vibrational temperature along the stagnation line for the reaction rate coefficients considered. Again, the results in 11 are normalized as a percentage of the standoff distance of the shock, allowing for direct comparison between different values of the reaction rate coefficient. The left and right bounds are the post-shock and surface locations respectively.

Figure 11 depicts a region of elevated temperature for $C_{f,c}$ > 2x10^4. This region experiences a peak temperature rise roughly 2500 K above the non-reacting solutions. This peak temperature occurs at the same location as the peak concentration of aluminum oxide, as discussed with Figure 5. A temperature rise at this location is expected due to the exothermic nature of aluminum oxide production and is responsible for dramatically increasing the incident heat flux as previously discussed.

For $C_{f,c}$ = 2x10^1, the peak temperature rise is approximately 1000 K, though the temperature gradient near the surface is similar to those for higher reaction rate coefficients. As discussed with figure 10, the peak formation of

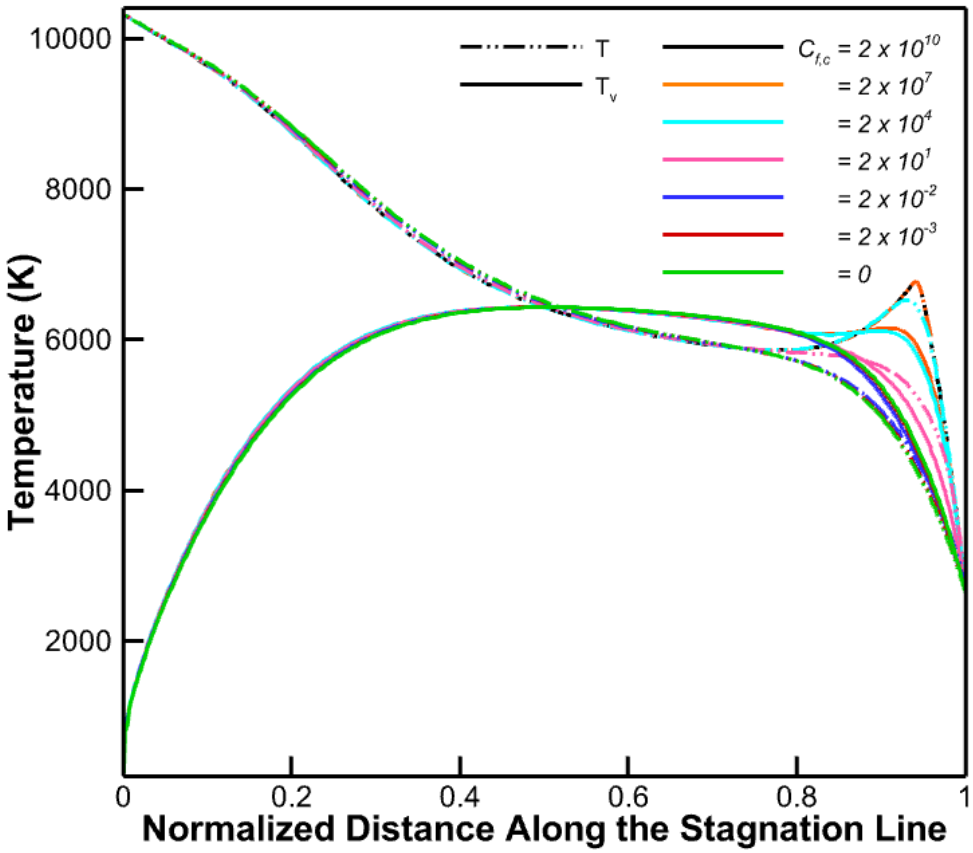

Fig. 11 Normalized stagnation line profile of temperature and vibrational temperature for different reaction rates.

aluminum oxide occurs near the surface and drops off further along the boundary-layer for $C_{f,c} = 2\text{x}10^{1}$, confining the effects of aluminum oxide formation to the surface. Because the concentration of aluminum oxide near the surface is the same for $C_{f,c} = 2\text{x}10^{1}$ and for higher reaction rate coefficients, the heat released due to the reaction and the heat that is carried to the surface remains similar. Therefore, the incident heat flux is similar between these solutions despite the smaller peak temperature rise and the lower temperature gradient further out towards the edge of the boundary-layer. The lower reaction rates exhibit temperature profiles along the stagnation line similar to the non-reacting case.

The vibrational temperature also changes similarly, as the region of elevated temperature in turn leads to greater molecular excitation. The effect on vibrational temperature is not as pronounced, however, as the nonequilibrium state of vibrational excitation causes the vibrational temperature to lag behind the changes in flow temperature.

Table 3 details how the performance of evaporative transpiration TPS are affected by changes in the reaction rate coefficient. Table 3 also shows how the stagnation point mass fraction of aluminum and aluminum oxide vary with changes in reaction rate coefficient.

Table 3 shows that, for $C_{f,c} \geq 2\text{x}10^{-2}$, the oxidation reaction becomes significant and additional coolant is required to replace the coolant that is oxidized. By $C_{f,c} = 2\text{x}10^{1}$, the maximum coolant mass flux at the stagnation point is required of the transpiration TPS. This is because, as discussed with Figure 10, there is complete consumption of atomic oxygen for this reaction rate coefficient. Complete consumption of oxygen corresponds to the maximum possible increase in coolant mass flux due to the oxidation reaction because the reaction cannot progress past this state. Additionally, for $C_{f,c} \geq 2\text{x}10^{1}$, the mass fraction of Al begins to decrease compared to slower reactions. This occurs

because more aluminum oxide diffuses towards the surface at higher reaction rates. The increased presence of aluminum oxide decreases the mass fraction of aluminum as discussed with Figure 4. The reaction rate coefficient of $C_{f,c}$ = $2\text{x}10^{-2}$ experiences the largest stagnation point mass fraction of aluminum because the reaction rate is large enough for the oxidation reaction to occur but not so large as to produce enough aluminum oxide to dominate the flow field. As a result, additional aluminum is vaporised to react with oxygen, but the additional aluminum coexists with oxygen in a nonequilibrium state at the stagnation point as discussed with Figure 10.

With a value of $C_{f,c} = 2\text{x}10^{-2}$, the stagnation point mass flux is 1.67 kg/m^2-s. This is larger than the mass flux of 0.987 kg/m^2-s for the non-reacting solution but smaller than the mass flux of 2.23 kg/m^2-s for the equilibrium flow solutions with $C_{f,c} \geq 2\text{x}10^{1}$. The required coolant mass flux for $C_{f,c} = 2\text{x}10^{-2}$ is in between the values of 0.987 and 2.23 kg/m^2-s because this reaction rate coefficient corresponds to nonequilbrium flow, while the other mass fluxes correspond to frozen and equilibrium flow, respectively. The required coolant mass flux for $C_{f,c} = 2\text{x}10^{-2}$ remains closer to the required coolant mass flux for solutions with faster reaction rates. This is because a majority of the oxygen in the flow is still consumed when $C_{f,c} = 2\text{x}10^{-2}$, producing aluminum oxide in an exothermic reaction and increasing the temperature gradient near the leading edge surface. The mass flux for $C_{f,c} = 2\text{x}10^{-3}$ is 1.15 kg/m^2-s. This value is slightly larger than the results for non-reacting flow because the oxidation reaction still occurs for a finite reaction rate coefficient, but at a slow and nearly insignificant rate.

Figure 12 presents the resulting incident and evaporative heat fluxes along the leading edge surface as the reaction rate coefficient is varied. Additionally shown is the cooling heat flux for comparison to the incident heat flux. The cooling heat flux is defined as the evaporative heat flux plus the radiation heat flux. Other heat fluxes, such as the radiation heat flux or recombination heat flux, are not explicitly shown because they are either nearly constant between

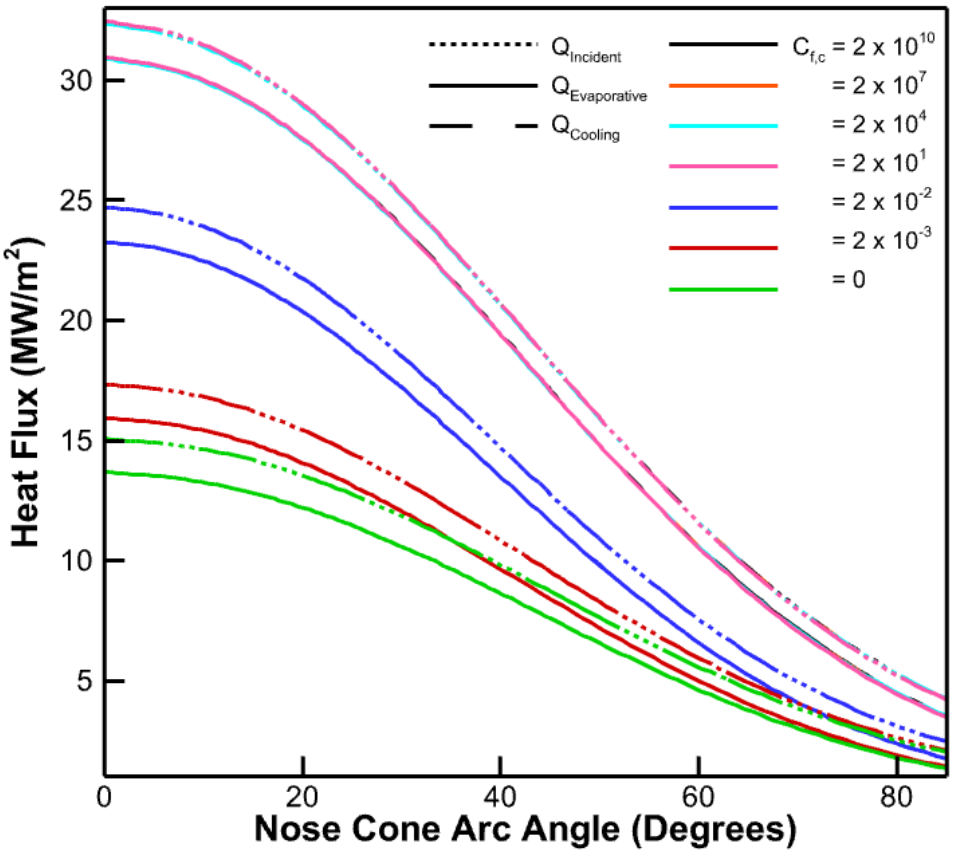

Fig. 12 Surface heat fluxes for different reaction rates.

trials or insignificant. The left-most boundary is the stagnation location, and traveling rightward corresponds to traveling circumferentially along the leading edge surface.

Previous results are reinforced through Figure 12. The region of elevated temperature from Figure 11 leads to an increase in the temperature gradient inside the boundary-layer, and therefore an increase in the incident heat flux by equation 14. The evaporative heat flux must then increase to counteract the increased incident heat flux caused by the exothermic oxidation reaction. This balancing of heat fluxes keeps the surface temperature near the saturation temperature of the coolant, as required by equations 16 and 17, but increases the required coolant mass fluxes as reported in Table 3. These processes can be seen to relate visually in Figure 12. A change in reaction rate coefficient leads to a change in both the incident and evaporative heat fluxes. A change in the incident heat flux must be offset by an equal change in the evaporative heat flux and vice versa, as the other heat fluxes do not change significantly. The incident and cooling heat fluxes can be seen to be equal in all cases. Once again, all results with large $C_{f,c}$ are similar. The surface heat fluxes do not begin to distinguish themselves until $C_{f,c} \leq 2\text{x}10^{-2}$. This corresponds to the mass fluxes reported in Table 3, where the mass fluxes for reaction rates $C_{f,c} \geq 2\text{x}10^{1}$ are all equivalent, and only begin to distinguish themselves for $C_{f,c} \leq 2\text{x}10^{-2}$.

Based on these results, if the conditions for an oxidation reaction to occur are met, then the oxidation reaction will lead to an increase in the incident heat flux along the leading edge surface. This results in an increase in both the evaporative heat flux and the coolant mass flux, while the surface temperature remains nearly unchanged.

Table 3 Comparison of stagnation point properties for different reaction rates

	$C_f, c = 2\text{x}10^{10}$	$2\text{x}10^{7}$	$2\text{x}10^{4}$	$2\text{x}10^{1}$	$2\text{x}10^{-2}$	$2\text{x}10^{-3}$	0
Mass Fraction of Al	0.173	0.174	0.175	0.186	0.192	0.187	0.186
Mass Fraction of AlO	0.335	0.335	0.334	0.321	0.177	0.044	0
Coolant Mass Flux (kg/m^2-s)	2.23	2.23	2.23	2.23	1.67	1.15	0.987

VII. Conclusion

Because one of the main limiting design consideration for hypersonic flight vehicles is the severe incident heat fluxes present during atmospheric hypersonic flight, research into more effective TPS is desired. Evaporative transpiration TPS are desirable because they function without degrading the leading edge surface and can maintain sharp leading edge geometry for high lift-to-drag ratios. This study has expanded on the work of Ko et al. (2024) [5] to further explore the limits of evaporative transpiration TPS. Specifically, this study investigates the effects of exothermic coolant oxidation reactions on evaporative transpiration TPS performance. This is accomplished through DNS studies of an evaporative transpiration TPS employing aluminum as the coolant material along the leading edge of a 3.1 mm nose tip radius flying at Mach 15 and an altitude of 30 km.

After the initial validation study of the new DNS code used to simulate the evaporative transpiration TPS, a study is conducted to determine the effect of coolant oxidation on the performance of the evaporative transpiration TPS. It is found that coolant oxidation led to roughly a twofold increase in the required coolant mass flux at the stagnation point. This is because the exothermic oxidation reaction increases the temperature gradient in the boundary-layer, leading to an increased incident heat flux acting along the leading edge surface. In order to counteract this increased incident heat flux, the evaporative heat flux must increase through increased coolant mass flux. Therefore, if the coolant may oxidise, the effects of coolant oxidation must be accounted for during the design of evaporative transpiration TPS. The performance drawbacks of coolant oxidation are roughly equivalent to a one-third reduction in the coolant latent heat of vaporization for aluminum. While the performance drawbacks of coolant oxidation are significant, coolants with low enough molar masses or high enough latent heats of vaporization can compensate for their decreased cooling potential when compared to other coolants with higher molar masses or lower latent heats of vaporization. Additionally, oxidation reactions and recombination of atomic oxygen cannot occur at the leading edge surface if all oxygen reacts before reaching the surface. Therefore, it is valid to assume that there is no oxidation of liquid coolant or recombination of atomic oxygen at the surface.

Finally, the relationship between the reaction rate of coolant oxidation reactions and evaporative transpiration TPS performance is investigated. It is shown that oxidation reactions are likely to remain in a state of equilibrium or frozen flow. This is because the nonequilibrium condition only exists over a narrow range of slow reaction rates, spanning three

orders of magnitude. Even for reaction rates as low as 10^{-9} times their accepted values, conditions heavily favored coolant oxidation in an equilibrium state with complete consumption of oxygen. As a result, oxidation reactions occur in an equilibrium state if there are favorable equilibrium constants and reaction rates, and if there are available reacting species. Because oxidation reactions occur so readily, they cannot be neglected. Exothermic oxidation reactions lead to an increased incident heat flux and a corresponding increase in the required coolant mass flux. This leads to an increase in the evaporative coolant flux to counteract the increased incident heat flux, while the surface temperature remains nearly unchanged. Because oxidation reactions occur so readily and have a substantial impact on evaporative TPS performance, the oxidation of coolant species must be considered during the design of evaporative transpiration TPS.

With these results, a step has been taken toward one day implementing evaporative transpiration TPS capable of providing large cooling fluxes without experiencing surface degradation of the leading edge. However, more work is needed to fully detail the effects of coolant oxidation on evaporative transpiration TPS performance. Because the flow field in this study is oxygen-depleted near the leading edge surface, additional oxidation reactions may be of importance. A specific reaction of interest is the formation of aluminum(I) oxide, Al_2O, expected to form in significant qualities due to the oxygen-depleted flow environment. Formation of this oxide may have a significant impact on evaporative transpiration TPS performance, as twice the additional aluminum mass flux may be required to form this oxide as is required to form aluminum oxide, AlO, considered in this study.

Acknowledgments

A. Mannion thanks ACCESS (Advanced Cyberinfrastructure Coordination Ecosystem: Services & Support) and the teams responsible for maintaining the Purdue ANVIL super computers. Without the core-hours and computational resources provided this research could not have been completed. A. Mannion also thanks ChatGPT, Copilot, Grammarly, and Writeful as artificial intelligence tools used to assist in correcting grammatical and spelling mistakes in rough drafts of this work.

References

[1] Van Driest, E. R., "The Problem of Aerodynamic Heating," *Inst. of the Aeronautical Sciences*, 1956.

[2] Fay, J. A., and Riddell, F. R., "Theory of Stagnation Point Heat Transfer in Dissociated Air," *Journal of the Aerospace Sciences*, Vol. 25, No. 2, 1958, pp. 73–85. https://doi.org/10.2514/8.7517.

[3] Tran, H., Johnson, C., Rasky, D., Hui, F., Hsu, M.-T., and Chen, Y., "Phenolic Impregnated Carbon Ablators (PICA) for Discovery class missions," *31st Thermophysics Conference*, 1996. https://doi.org/10.2514/6.1996-1911.

[4] Anderson Jr, J. D., *Modern Compressible Flow: With Historical Perspective*, McGraw-Hill, 2004.

[5] Ko, D., and Mannion, A., "Parametric study of transpiration cooling using oxides for sharp hypersonic leading edges," *Journal of Thermophysics and Heat Transfer*, 2024. https://doi.org/10.2514/1.T6991.

[6] Sahu, R., Tropina, A., Andrienko, D., and Miles, R., "Cesium seeding for effective electron transpiration cooling in hypersonic flows," *Plasma Sources Science and Technology*, Vol. 31, No. 3, 2022, p. 035001. https://doi.org/10.1088/1361-6595/ac4ecc.

[7] Weston, K. C., "The Stagnation-point Boundary Layer with Suction and Injection in Equilibrium Dissociating Air," Tech. Rep. NASA-TN-D-3889, Dec. 1968.

[8] Henline, W. D., "Transpiration cooling of hypersonic blunt bodies with finite rate surface reactions," Tech. Rep. A-89018, Feb. 1989.

[9] Otsu, H., Fujita, K., and Ito, T., "Application of the Transpiration Cooling Method for Reentry Vehicles," *45th AIAA Aerospace Sciences Meeting and Exhibit*, 2007. https://doi.org/10.2514/6.2007-1209.

[10] Huang, G., Zhu, Y., Liao, Z., and Jiang, P.-X., "Experimental investigation of self-pumping internal transpiration cooling," *International Journal of Heat and Mass Transfer*, Vol. 123, 2018, pp. 514–522. https://doi.org/10.1016/j.ijheatmasstransfer.2018.02.046.

[11] Wu, N., Wang, J., He, F., Chen, L., and Ai, B., "Optimization transpiration cooling of nose cone with non-uniform permeability," *International Journal of Heat and Mass Transfer*, Vol. 127, 2018, pp. 882–891. https://doi.org/10.1016/j.ijheatmasstransfer.2018.07.134.

[12] Gulli, S., and Maddalena, L., "Arc-Jet Testing of a Variable-Transpiration-Cooled and Uncoated Carbon–Carbon Nose Cone," *Journal of Spacecraft and Rockets*, Vol. 56, No. 3, 2019, pp. 780–788. https://doi.org/10.2514/1.A34176.

[13] He, F., Wu, N., Ran, F., and Wang, J., "Numerical investigation on the transpiration cooling of three-dimensional hypersonic inlet," *Aerospace Science and Technology*, Vol. 106, 2020, p. 106152. https://doi.org/10.1016/j.ast.2020.106152.

[14] Ifti, H. S., Hermann, T., McGilvray, M., and Merrifield, J., "Numerical Simulation of Transpiration Cooling in a Laminar Hypersonic Boundary Layer," *Journal of Spacecraft and Rockets*, Vol. 59, No. 5, 2022, pp. 1726–1735. https://doi.org/10.2514/1.A35325.

[15] Ewenz Rocher, M., Hermann, T., McGilvray, M., and Gollan, R., "Correlation for Species Concentration on a Hypersonic Stagnation Point with Mass Injection," *AIAA Journal*, Vol. 60, No. 5, 2022, pp. 2798–2809. https://doi.org/10.2514/1.J061159.

[16] van Foreest, A., Sippel, M., Gülhan, A., Esser, B., Ambrosius, B. A. C., and Sudmeijer, K., "Transpiration Cooling Using Liquid Water," *Journal of Thermophysics and Heat Transfer*, Vol. 23, No. 4, 2009, pp. 693–702. https://doi.org/10.2514/1.39070.

[17] Luo, S., Miao, Z., Liu, J., Song, J., Xi, W., and Liu, C., "Effects of Coolants of Double Layer Transpiration Cooling System in the Leading Edge of a Hypersonic Vehicle. Front," *Front. Energy Res*, 2021. https://doi.org/10.3389/fenrg.2021.756820.

[18] Scala, S. M., and Vidale, G. L., "Vaporization processes in the hypersonic laminar boundary layer," *International Journal of Heat and Mass Transfer*, Vol. 1, No. 1, 1960, pp. 4–22. https://doi.org/10.1016/0017-9310(60)90003-X.

[19] Park, C., "On convergence of computation of chemically reacting flows," *AIAA Paper 1985-0247*, 1985. https://doi.org/10.2514/6.1985-247.

[20] Park, C., *Nonequilibrium hypersonic aerothermodynamics*, Wiley, New York, 1990.

[21] Bhutta, B. A., and Lewis, C. H., "Low-to-high altitude predictions of three-dimensional ablative re-entry flowfields," *Journal of Spacecraft and Rockets*, Vol. 30, No. 4, 1993, pp. 395–403. https://doi.org/10.2514/3.25544.

[22] Johnston, C. O., "Influence of Coupled Radiation and Ablation on Meteor Entries," *47th AIAA Thermophysics Conference*, 2017. https://doi.org/10.2514/6.2017-4533.

[23] McBride, B., Heimel, S., Ehlers, J., and Gordon, S., *Thermodynamic Properties to 6000 K for 210 Substances Involving the First 18 Elements*, NASA SP-3001, Office of Scientific and Technical Information. National Aeronautics and Space Administration, 1963.

[24] Malcolm, W., and Chase, J., "NIST-JANAF thermochemical tables," *J. Phys. Chem. Ref. Data*, Vol. 9, 1998.

[25] Blottner, F. G., Johnson, M., and Ellis, M., "CHEMICALLY REACTING VISCOUS FLOW PROGRAM FOR MULTI-COMPONENT GAS MIXTURES." Tech. Rep. SC-RR-70-754, Sandia Labs., Albuquerque, N. Mex., Jan. 1971. https://doi.org/10.2172/4658539.

[26] Gupta, R., Lee, K.-P., Moos, J., and Sutton, K., "Viscous-shock-layer solutions with coupled radiation and ablation injection for earth entry," *5th Joint Thermophysics and Heat Transfer Conference*, 1990, p. 1697.

[27] Hirschfelder, J. O., Curtiss, C. F., and Bird, R. B., *The Molecular Theory of Gases and Liquids*, Wiley, 1954.

[28] Breck, D. W., *Zeolite molecular sieves: structure, chemistry, and use*, John Wiley & Sons, 1973.

[29] Wilke, C. R., "A Viscosity Equation for Gas Mixtures," *The Journal of Chemical Physics*, Vol. 18, No. 4, 1950, pp. 517–519.

[30] Mortensen, C. H., "Effects of Thermochemical Nonequilibrium on Hypersonic Boundary-Layer Instability in the Presence of Surface Ablation or Isolated Two-Dimensional Roughness," Ph.D. thesis, University of California Los Angeles, United States – California, 2015.

[31] X., Z., "High-Order Finite-Dierence Schemes for Numerical Simulation of Hypersonic Boundary-Layer Transition," *Journal of Computational Physics*, Vol. 144, No. 2, 1998, pp. 662–709. https://doi.org/10.1006/jcph.1998.6010.

[32] J., W., "Low-Storage Runge-Kutta Schemes," *Journal of Computational Physics*, Vol. 35, No. 1, 1980, pp. 48–56.

[33] Ma, Y., and Zhong, X., "Numerical Simulation of Receptivity and Stability of Nonequilibrium Reacting Hypersonic Boundary Layers," *AIAA 39th Aerospace Sconces Meeting and Exhibit*, 2001. https://doi.org/10.2514/6.2001-892.